A Multiharmonics Suppression Backstepping Extended State Observer for the PMSM Electrolytic Capacitorless Drives Sensorless Control

Yuehan Li, Zhonggang Yin, *Member, IEEE*, Dongsheng Yuan, Yanqing Zhang, *Member, IEEE*, Yixuan Gao, and Hui Yang

***Abstract*—The electrolytic capacitorless driver has a longer service life and higher reliability than traditional permanent magnet synchronous motor (PMSM) drivers. However, the ac component in the dc-link voltage will generate corresponding harmonics in the back electromotive force (BEMF), which will reduce the control accuracy of sensorless. The traditional extended state observer exhibits low-pass filtering characteristics, making it difficult to accurately estimate the BEMF that varies sinusoidally and effectively suppress the BEMF harmonics. Therefore, a multiharmonics suppression backstepping extended state observer (M-BESO) is proposed in this article. The BESO is designed in reverse according to the amplitude frequency characteristics of the bandpass filter, so that the center frequency changes with the motor frequency. Then, the complex coefficient module is introduced into the structure of BESO to eliminate the harmonics in the BEMF caused by the fluctuation component of the dc-link voltage. To mitigate the position estimation error when the motor speed changes rapidly, an improved phase locked loop based on third-order extended state observer is designed. Finally, the proposed method is verified on a self-built experimental platform based on the PMSM electrolytic capacitorless drives.**

***Index Terms*—Electrolytic capacitorless drives, multiharmonics suppression backstepping extended state observer (M-BESO), permanent magnet synchronous motor (PMSM), sensorless control.**

I. Introduction

COMPARED with other types of motors, permanent magnet synchronous motor (PMSM) has the characteristics of high-power density, high efficiency, and good speed regulation performance, which makes it have certain advantages in aerospace, industrial production, electric vehicles, and other fields [1], [2], [3]. However, for the traditional motor driver, the electrolytic capacitor on the dc-link is very sensitive to the ambient temperature [4]. With the increase of environmental temperature, the service life of electrolytic capacitors will decrease, which will greatly affect the reliability of traditional motor drive systems. The film capacitors have good stability and long service life. Therefore, replacing large-capacity electrolytic capacitors with small-capacity film capacitors in the electrolytic capacitorless drives has become a research hotspot for many scholars. Although electrolytic capacitorless drives can improve their service life and power density, their insufficient dc-link energy storage capacity also brings many problems. The current research direction mainly focuses on *LC* resonance suppression, grid side power quality improvement, motor side beat phenomenon suppression, dc-link overvoltage suppression, and other aspects [5], [6], [7].

The high performance control of PMSM is inseparable from accurate position and speed information. Installing mechanical sensors, such as encoders or rotary transformers, will increase the cost of the drive and reduce reliability. Therefore, to further improve the reliability of electrolytic capacitorless drives, high-precision sensorless control strategies will be indispensable. At present, the sensorless control strategy of PMSM can be divided into saliency-based method applied in low-speed region and model-based method applied in medium high-speed region [8]. The former mainly includes high-frequency signal injection methods, which can be divided into rotational signal injection [9] and pulsating signal injection [10], closely related to the saliency of the motor; the latter is achieved by utilizing the back electromotive force (BEMF) or magnetic flux information of the motor. The sensorless methods applied in medium and high speed region mainly include model reference adaptive system (MRAS) [11], extended Kalman filter (EKF) [12], sliding mode observer (SMO) [13], extended state observer (ESO), etc. To achieve high-precision sensorless control, MRAS relies on precise motor parameters and has poor robustness to motor parameter mismatches. The EKF considers the impact of modeling errors and measurement noise on the system in its design, and has strong noise suppression capabilities, but its algorithm requires a

Received 31 December 2024; revised 21 March 2025; accepted 25 March 2025. Date of publication 1 April 2025; date of current version 26 May 2025. This work was supported in part by the Research Fund for the National Natural Science Foundation of China under Grant 52177194, Grant 52107206, and Grant 52207016, and in part by the China Postdoctoral Science Foundation under Grant 2020M683524. Recommended for publication by Associate Editor F. W. Fuchs. *(Corresponding author: Zhonggang Yin.)*

The authors are with the Department of Electrical Engineering, Xi'an University of Technology, Xi'an 710048, China (e-mail: 1221910015@stu.xaut.edu.cn; zhgyin@xaut.edu.cn; dsyuan@xaut.edu.cn; zhangyanqing@xaut.edu.cn; 1221910014@stu.xaut.edu.cn; ivyyang@xaut.edu.cn).

Color versions of one or more figures in this article are available at https://doi.org/10.1109/TPEL.2025.3556854.

Digital Object Identifier 10.1109/TPEL.2025.3556854

large amount of computation. The SMO has inherent chattering problems, which can increase position estimation errors.

The ESO does not rely on system models and has advantages, such as high accuracy and the ability, to estimate unknown disturbances [14]. Therefore, some researchers use ESO to estimate BEMF. The ESO includes the nonlinear ESO (NESO) and the linear ESO (LESO). The stability analysis and parameter setting rules of the LESO are simple and practical, and have been recognized by many scholars. However, the NESO analysis is very complex [15]. According to the amplitude frequency characteristics of the transfer function of the LESO, LESO has the function of low-pass filtering for the estimated output signal. When LESO is applied to sensorless control, there is a phase error between the estimated BEMF and the actual BEMF, resulting in position estimation error. Adjusting the bandwidth of LESO will create a contradiction between reducing phase error and noise suppression. In response to the above issues, scholars have proposed many different structures of ESO [16], [17], [18]. In [16], an IESO based on bandwidth adaptive adjustment was designed to achieve good BEMF estimation performance over a wide operating range. However, the estimated BEMF still has phase lag. In [17], the disturbance estimation loop in LESO consists of pure integral and sine disturbance generalized integral estimators (SDGIE). The SDGIE is used to estimate the BEMF that varies sinusoidally, and its center frequency changes adaptively with the motor frequency. In [18], an enhanced LESO using a quasi-resonant controller was proposed. Adding a quasi-resonant controller to the BEMF estimation circuit of LESO ensures that the estimated BEMF closely follows the actual BEMF, effectively alleviating phase lag. Adding sinusoidal BEMF estimation module to LESO can alleviate the phase lag of estimated BEMF. However, this leads to the increase of observer order, and the improved LESO still struggles to suppress the dc component in the BEMF.

In recent years, the strategy of using predesigned transfer functions to reverse construct BEMF observers has been proposed. In [19], a minimum order BEMF observer was proposed. In this article, a transfer function is constructed. According to its amplitude frequency characteristics, the dc bias can be suppressed, and there is no phase shift and amplitude attenuation at the center frequency. Then, using the backstepping method, a BEMF observer is proposed to accurately estimate the BEMF while suppressing the dc component. In [20], a transfer function for an observer with harmonic suppression capability was proposed. Then, an adaptive generalized complex vector observer was reverse designed to accurately estimate the BEMF of the motor, while effectively suppressing dc bias and low order harmonics. This strategy of reverse designing observers based on expected transfer functions has also brought new ideas to the structural design of LESO.

For PMSM electrolytic capacitorless drives, the dc-link voltage will contain a fluctuation component six times the grid frequency, which will ultimately exhibit harmonics with angular velocity $\omega_e \pm 6k\omega_g$ in the extended BEMF [21]. The frequency of these harmonics varies with the motor frequency, which increases the position estimation error. To eliminate harmonics in the BEMF, the usual method is to connect filters in series after estimating the BEMF, such as second-order generalized integrators, notch filters, adaptive training control filters, and complex coefficient filters [22], [23], [24], [25]. Another method is to construct an observer with a novel structure that possesses corresponding harmonic suppression capabilities. In [26], a subordinative structure full order BEMF observer was proposed to estimate the fundamental component of BEMF while suppressing multiple harmonics. The structure of the observer has been redesigned to separate the fundamental and harmonic components, improving the accuracy of sensorless control. In [27], a BEMF observer was proposed in the estimated *dq*-axis coordinate system. Adding a harmonic estimation module to the traditional observer structure effectively extracts the BEMF fundamental component manifested as a dc component.

The traditional extended state observer (TESO) is difficult to accurately estimate the BEMF of sinusoidal variations and effectively suppress the BEMF harmonics caused by fluctuating dc-link voltages. Therefore, the sensorless method for electrolytic capacitorless driver based on multiharmonic suppression backstepping extended state observer (M-BESO) is proposed in this article. The contributions of this article are as follows.

1) Based on the transfer function of the second-order bandpass filter, the backstepping extended state observer (BESO) is obtained through reverse design. Compared to the TESO, the BESO can accurately estimate BEMF and has the ability to suppress dc bias.
2) The main contribution of this article is that the proposed M-BESO can accurately estimate BEMF while effectively suppressing BEMF harmonics generated by the ac component in the dc-link voltage. Thereby further improving the accuracy of position estimation. The M-BESO is obtained by introducing corresponding complex coefficient module into the BESO.
3) When the input is a ramp frequency signal, traditional phase-locked loops (TPLL) will cause position errors. Therefore, to improve the position estimation accuracy when the motor operating frequency changes rapidly, an improved phase-locked loop (IPLL) is designed based on third-order ESO.

Finally, the proposed method is verified by the experimental platform of the 2 kW PMSM based on electrolytic capacitor-less driver.

II. Sensorless Control Method Based on the TESO

A. Mathematical Model of PMSM

In the two-phase stationary coordinate system, the PMSM model is usually constructed as

$$\begin{bmatrix} v_{s\alpha} \\ v_{s\beta} \end{bmatrix} = \begin{bmatrix} R_s & 0 \\ 0 & R_s \end{bmatrix} \begin{bmatrix} i_{s\alpha} \\ i_{s\beta} \end{bmatrix} + \begin{bmatrix} pL_q & 0 \\ 0 & pL_q \end{bmatrix} \begin{bmatrix} i_{s\alpha} \\ i_{s\beta} \end{bmatrix} + \begin{bmatrix} e_{s\alpha} \\ e_{s\beta} \end{bmatrix} \tag{1}$$

where $i_{s\alpha}$ and $i_{s\beta}$ are the current of $\alpha\beta$-axis, respectively; $v_{s\alpha}$ and $v_{s\beta}$ are the $\alpha\beta$-axis voltages, respectively; R_s, L_q, and p represent the stator resistance, q-axis inductance, and differential

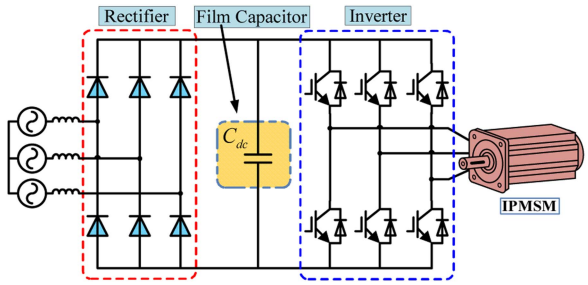

Fig. 1. Main circuit topology of the electrolytic capacitorless drives.

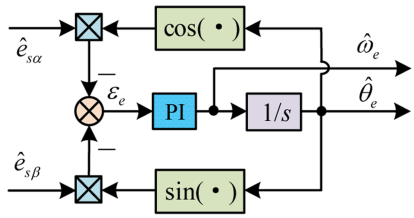

Fig. 2. Structure diagram of the TPLL.

operator, respectively. $e_{s\alpha}$ and $e_{s\beta}$ are the BEMF of the $\alpha\beta$-axis, respectively, which can be described as

$$\begin{bmatrix} e_{s\alpha} \\ e_{s\beta} \end{bmatrix} = \omega_e \cdot \left[\varphi_f + (L_d - L_q)\, i_d\right] \begin{bmatrix} -\sin\theta_e \\ \cos\theta_e \end{bmatrix} \tag{2}$$

where θ_e and ω_e are rotor position and the electrical angular velocity, respectively; L_d, φ_f, and id represent d-axis inductance, the permanent magnet magnetic flux, and d-axis current, respectively.

B. Harmonic Analysis of the Electrolytic Capacitorless Drives

Fig. 1 depicts the main circuit topology of the PMSM electrolytic capacitorless drives. In [19], the dc-link voltage of the electrolytic capacitorless driver is

$$v_{\text{dc}} = V_{\text{dc}} + \sum_{k=1}^{n} V_{\text{dc}k} \sin\left(6k\omega_g t + \varphi_{\text{dc}k}\right). \tag{3}$$

The *dq*-axis current derived from (3) is

$$\begin{bmatrix} i_d \\ i_q \end{bmatrix} = \begin{bmatrix} I_1 \sin\varphi_1 + \sum_{k=1}^{n} I_{dck} \left[\mp\cos\left(\pm 6k\omega_g t + \varphi_{\pm ik}\right)\right] \\ -I_1 \cos\varphi_1 - \sum_{k=1}^{n} I_{dck} \left[\mp\sin\left(\pm 6k\omega_g t + \varphi_{\pm ik}\right)\right] \end{bmatrix} \tag{4}$$

where φ_1 and I_1 are the fundamental phase and amplitude of the A-phase current; $\varphi_{\pm ik}$ and I_{dck} are the initial phase and amplitude of harmonics in the dq-axis current caused by the kth harmonic in the dc-link voltage.

According to (2) and (4), the amplitude of $\alpha\beta$-axis BEMF of the motor can be represented as

$$\begin{aligned} E_{\text{emf}} &= \omega_e \cdot \left[\varphi_f + (L_d - L_q)\, i_d\right] \\ &= E_{\text{emf},0} + \sum_{k=1}^{n} E_{\text{emf},\pm 6k\omega_g} \left[\cos\left(\pm 6k\omega_g t + \varphi_{\pm ik}\right)\right] \end{aligned} \tag{5}$$

where

$$\begin{cases} E_{\text{emf},0} = \omega_e \left[\varphi_f + (L_d - L_q)\, I_1 \cdot \sin\varphi_1\right] \\ E_{\text{emf},\pm 6k\omega_g} = \mp\left(\omega_e \mp 6\omega_g\right)\left(L_d - L_q\right) \cdot I_{\text{dc}k} \end{cases} \tag{6}$$

where $E_{\text{emf},0}$ is the fundamental component of BEMF amplitude, and $E_{\text{emf},\pm 6k\omega_g}$ is the amplitude of the BEMF harmonic caused by the kth harmonic in the dc-link voltage.

According to (2) and (5), the BEMF of the $\alpha\beta$-axis can be obtained as follows:

$$\begin{aligned} e_{s\alpha} &= -E_{\text{emf}} \sin\omega_e t \\ &= -E_{\text{emf},0} \sin\omega_e t - \sum_{k=1}^{n} \frac{E_{\text{emf},\pm 6k\omega_g}}{2} \\ &\quad \left\{\sin\left[\left(\omega_e \pm 6k\omega_g\right) t + \varphi_{\pm ik}\right]\right. \\ &\quad \left. -\sin\left[\left(\omega_e \mp 6k\omega_g\right) t - \varphi_{\pm ik}\right]\right\} \\ e_{s\beta} &= E_{\text{emf}} \cos\omega_e t \\ &= E_{\text{emf},0} \cos\omega_e t + \sum_{k=1}^{n} \frac{E_{\text{emf},\pm 6k\omega_g}}{2} \\ &\quad \left\{\cos\left[\left(\omega_e \pm 6k\omega_g\right) t + \varphi_{\pm ik}\right]\right. \\ &\quad \left. -\cos\left[\left(\omega_e \mp 6k\omega_g\right) t - \varphi_{\pm ik}\right]\right\}. \end{aligned} \tag{7}$$

According to (7), for the electrolytic capacitorless driver, the harmonics in the dc-link voltage will eventually generate harmonics in the motor BEMF. The angular velocity of the resulting BEMF harmonics is $\omega_e \pm 6k\omega_g$. Fig. 2 shows the structure of the TPLL. In sensorless control, PLL uses the estimated BEMF of $\alpha\beta$-axis to calculate the position and speed information. In PLL, the position error can be calculated as follows:

$$\begin{aligned} \varepsilon_e &= -e_{s\alpha} \cos\hat{\theta}_e - e_{s\beta} \sin\hat{\theta}_e \\ &= E_{\text{emf},0} \sin\left(\omega_e - \hat{\omega}_e\right) t + \sum_{k=1}^{n} E_{\text{emf},\pm 6k\omega_g} \\ &\quad \sin[(\omega_e - \hat{\omega}_e)t \pm 6k\omega_g t + \varphi_{\pm ik}] \\ &\approx \theta_e - \hat{\theta}_e + \sum_{k=1}^{n} E_{\text{emf},\pm 6k\omega_g} \sin\left[\pm 6k\omega_g t + \varphi_{\pm ik}\right]. \end{aligned} \tag{8}$$

According to (8), the dc-link voltage harmonics will eventually cause position error in the electrolytic capacitorless driver sensorless control. Therefore, the harmonics of estimated BEMF need to be suppressed in order to improve the accuracy of sensorless control.

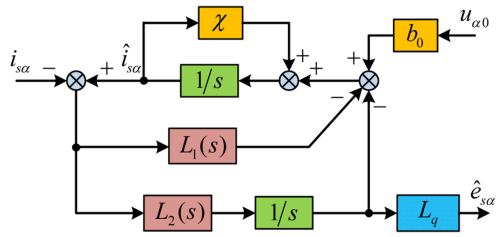

Fig. 3. Structure diagram of the TESO.

C. Design of the TESO

Equation (1) can be transformed into

$$\begin{cases} pi_{s\alpha} = \frac{1}{L_q}v_{s\alpha} - \frac{R_s}{L_q}i_{s\alpha} - \frac{1}{L_q}e_{s\alpha} \\ pi_{s\beta} = \frac{1}{L_q}v_{s\beta} - \frac{R_s}{L_q}i_{s\beta} - \frac{1}{L_q}e_{s\beta}. \end{cases} \tag{9}$$

In [17], the design method of TESO is mentioned according to the model of the first-order system. The following analysis will take the TESO design of the α-axis as an example. Considering (9), the system state variable $x_{\alpha 1}$, unknown disturbance variable $x_{\alpha 2}$, system input variable $u_{\alpha 0}$, and known disturbance variable $f(x_{\alpha 1}, t)$ in TESO can be defined as

$$\begin{cases} x_{\alpha 1} = i_{s\alpha} \\ x_{\alpha 2} = -e_{s\alpha}/L_q \\ f\left(x_{\alpha 1}, t\right) = -R_s \cdot i_\alpha / L_q = \chi i_\alpha \\ u_{\alpha 0} = v_{s\alpha}, b_0 = 1/L_q. \end{cases} \tag{10}$$

According to (9) and (10), the TESO based on the α-axis is

$$\begin{cases} \varepsilon_{\alpha 1} = \hat{x}_{\alpha 1} - i_{s\alpha} \\ p\hat{x}_{\alpha 1} = \hat{x}_{\alpha 2} + b_0 u_{\alpha 0} + f\left(\hat{x}_{\alpha 1}, t\right) - L_1(t) \cdot \varepsilon_{\alpha 1} \\ p\hat{x}_{\alpha 2} = -L_2(t) \cdot \varepsilon_{\alpha 1} \end{cases} \tag{11}$$

where $L_1(t)$ and $L_2(t)$ represent the gain expression of TESO. Fig. 3 is the structural diagram of TESO.

According to (11) and (9), the estimation error expression of TESO can be deduced as

$$\begin{cases} p\varepsilon_{\alpha 1} = \hat{x}_{\alpha 2} - x_{\alpha 2} + \chi\varepsilon_{\alpha 1} - L_1(t) \cdot \varepsilon_{\alpha 1} \\ p\hat{x}_{\alpha 2} = -L_2(t) \cdot \varepsilon_{\alpha 1}. \end{cases} \tag{12}$$

Based on the Laplace transform method, convert (12) into a frequency domain expression

$$\begin{cases} s\varepsilon_{\alpha 1}(s) = \hat{x}_{\alpha 2}(s) - x_{\alpha 2}(s) + [\chi - L_1(s)] \cdot \varepsilon_{\alpha 1}(s) \\ s\hat{x}_{\alpha 2}(s) = -L_2(s) \cdot \varepsilon_{\alpha 1}(s). \end{cases} \tag{13}$$

By transforming the two equations in (13) and eliminating $\varepsilon_{\alpha 1}(s)$, the transfer function of the unknown interference variable $\hat{x}_{\alpha 2}(s)$ to $x_{\alpha 2}(s)$ can be obtained

$$\frac{\hat{x}_{\alpha 2}(s)}{x_{\alpha 2}(s)} = \frac{L_2(s)}{s^2 + [L_1(s) - \chi] \cdot s + L_2(s)} \tag{14}$$

where $\hat{x}_{\alpha 2}(s) = -\hat{e}_{s\alpha}(s)/L_q$, $x_{\alpha 2}(s) = -e_{s\alpha}(s)/L_q$. When TESO tends to stabilize, the transfer function from $\hat{e}_{s\alpha}(s)$ to $e_{s\alpha}(s)$ can be expressed as

$$\frac{\hat{e}_{s\alpha}(s)}{e_{s\alpha}(s)} = \frac{L_2(s)}{s^2 + [L_1(s) - \chi] \cdot s + L_2(s)}. \tag{15}$$

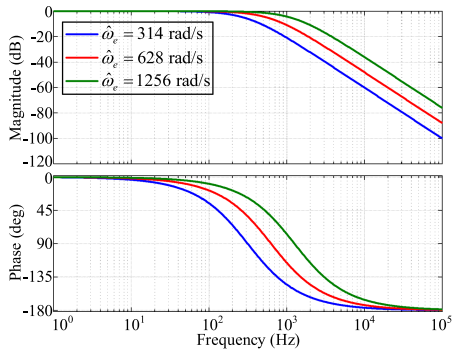

Fig. 4. Bode diagram of the TESO when the center frequency varies.

For TESO, $L_1(s)$ and $L_2(s)$ are constants. According to (15), its characteristic equation has two poles. Generally speaking, for ease of analysis, the two poles are set at the same point in the left half plane of the real axis. According to [18], L_1 and L_2 can be configured as

$$\begin{bmatrix} L_1 & L_2 \end{bmatrix}^T = \begin{bmatrix} 2\omega_0 + \chi & \omega_0^2 \end{bmatrix}^T. \tag{16}$$

Therefore, the transfer function from $\hat{e}_{s\alpha}(s)$ to $e_{s\alpha}(s)$ is further derived as

$$G_T(s) = \frac{\hat{e}_{s\alpha}(s)}{e_{s\alpha}(s)} = \frac{\omega_0^2}{(s + \omega_0)^2}. \tag{17}$$

The BEMF of PMSM is a sine component, and the response of $G_T(s)$ at the center frequency (i.e., motor operating frequency) ω_e can be expressed as (18). $G_T(s)$ exhibits second-order low-pass filtering characteristics. Fig. 4 shows the amplitude frequency characteristics of TESO when the center frequency varies. According to the bode diagram, the BEMF estimated by TESO has phase lag, which can cause position estimation errors. Increasing bandwidth ω_0 can reduce phase lag, but it will increase the noise in the estimated BEMF

$$G_T(j\omega_e) = \frac{\hat{e}_{s\alpha}(j\omega_e)}{e_{s\alpha}(j\omega_e)} = \frac{\omega_0^2}{(j\omega_e + \omega_0)^2} \neq 1. \tag{18}$$

III. Proposed M-BESO

A. Design of the BESO

The fundamental reason for the phase lag of BEMF estimated by TESO is that its transfer function presents the characteristics of low-pass filtering. There is no phase shift or amplitude attenuation at the center frequency of the output signal, and the signal other than the center frequency is attenuated, which is the characteristic of the expected ESO transfer function. According to (15), reasonable configuration of $L_1(s)$ and $L_2(s)$ can alter the transfer function of ESO. It is crucial to select a transfer function that meets the above requirements. The transfer function of the bandpass filter is as follows:

$$G_{\mathrm{BPF}}(s) = \frac{k_0 s}{s^2 + k_0 s + \omega_0^2} \tag{19}$$

where ω_0 and k_0 are the center frequency and coefficient of the bandpass filter, respectively.

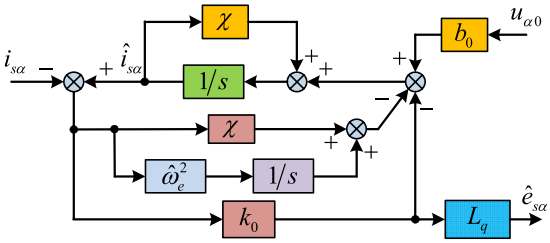

Fig. 5. Structure diagram of the proposed BESO.

The amplitude frequency characteristics of (19) meet the requirements for accurate estimation of BEMF by ESO. Therefore, using the backstepping method, design ESO in reverse according to (19). Equations (15) and (19) will be the same, with $L_1(s)$ and $L_2(s)$ configured as

$$\begin{cases} L_1(s) = \frac{1}{s}\hat{\omega}_e^2 + \chi \\ L_2(s) = k_0 s. \end{cases} \tag{20}$$

According to (20), derive the transfer function of the proposed BESO

$$G_B(s) = \frac{k_0 s}{s^2 + k_0 s + \hat{\omega}_e^2} \tag{21}$$

where $\hat{\omega}_e$ is the center frequency of BESO, which adaptively changes with the motor frequency. According to (20), the frequency domain expression of BESO can be obtained. Taking the α-axis as an example, it is shown as follows:

$$\begin{cases} \varepsilon_{\alpha 1}(s) = \hat{x}_{\alpha 1}(s) - i_{s\alpha}(s) \\ s\hat{x}_{\alpha 1}(s) = \hat{x}_{\alpha 2}(s) + b_0 u_{\alpha 0}(s) + \chi \hat{i}_{s\alpha}(s) \\ \qquad\qquad - \left(\frac{1}{s}\hat{\omega}_e^2 + \chi\right) \cdot \varepsilon_{\alpha 1}(s) \\ \hat{x}_{\alpha 2}(s) = -k_0 \cdot \varepsilon_{\alpha 1}(s). \end{cases} \tag{22}$$

Fig. 5 presents the structural diagram of the proposed BESO. Fig. 6(a) shows the bode diagram of $G_B(s)$ at $k_0 = 0.7\hat{\omega}_e$ and different center frequencies. According to bode diagram, the proposed BESO can accurately estimate the BEMF, ensure that there is no phase lag, and also has a certain ability to suppress harmonics and dc bias. Fig. 6(b) shows the bode plot of $G_B(s)$ at a center frequency of $\hat{\omega}_e = 314$ rad/s and different k_0. As shown in Fig. 6(b), the smaller the k_0, the stronger the harmonic suppression ability, but the dynamic response will deteriorate. For this reason, the coefficient k_0 of BESO needs to compromise between harmonic suppression and dynamic response.

B. Design of the M-BESO

The PMSM electrolytic capacitorless drives will ultimately generate harmonics with angular velocity $\omega_e \pm 6k\omega_g$ in BEMF. As the dc-link voltage fluctuation increases, the harmonic amplitude in BEMF will also correspondingly increase. However, the BESO needs to compromise between harmonic suppression and dynamic response. Therefore, to effectively suppress the BEMF harmonics caused by dc-link voltage, the M-BESO incorporating cross decoupling complex coefficient modules is proposed in this article.

The dc-link voltage mainly contains harmonics with angular velocity $6\omega_g$. Therefore, only the harmonic of angular velocity

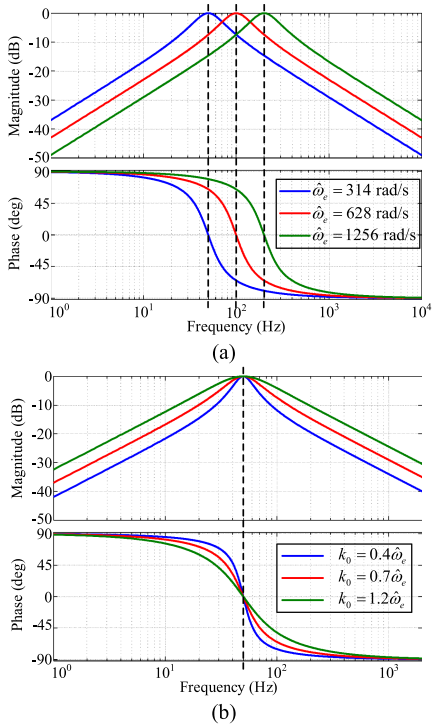

Fig. 6. Bode diagram of the transfer function of the BESO. (a) When $\hat{\omega}_e$ change. (b) When k_0 change.

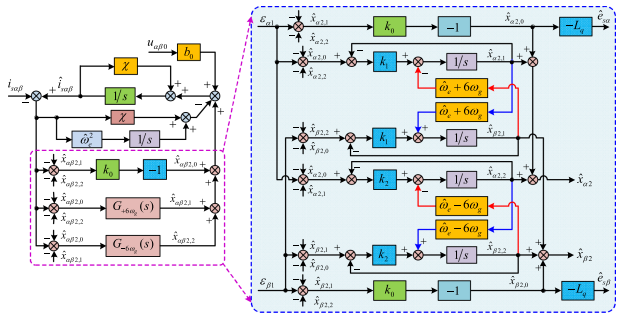

Fig. 7. Control structure diagram of the proposed M-BESO.

$\omega_e \pm 6\omega_g$ caused by the harmonic of the dc-link voltage in BEMF is considered.

The control structure diagram of the proposed M-BESO can be depicted as Fig. 7. Extract harmonics with angular velocity $\hat{\omega}_e \pm 6\omega_g$ in BEMF using the complex coefficient module. To accurately separate the fundamental and harmonics of the BEMF, a cross-decoupling method is adopted. In M-BESO, the fundamental and harmonics of BEMF are represented by the following frequency domain model:

$$\begin{cases} s\hat{x}_{\alpha 2,0}(s) = -L_2(s) \cdot [\varepsilon_{\alpha 1}(s) - \hat{x}_{\alpha 2,1}(s) - \hat{x}_{\alpha 2,2}(s)] \\ \hat{x}_{\alpha 2,1}(s) = G_{+6\omega_g}(s) \cdot [\varepsilon_{\alpha 1}(s) - \hat{x}_{\alpha 2,0}(s) - \hat{x}_{\alpha 2,2}(s)] \\ \hat{x}_{\alpha 2,2}(s) = G_{-6\omega_g}(s) \cdot [\varepsilon_{\alpha 1}(s) - \hat{x}_{\alpha 2,0}(s) - \hat{x}_{\alpha 2,1}(s)] \end{cases} \tag{23}$$

where

$$\begin{cases} G_{+6\omega_g}(s) = \frac{k_1}{s - j(\hat{\omega}_e + 6\omega_g) + k_1} \\ G_{-6\omega_g}(s) = \frac{k_2}{s - j(\hat{\omega}_e - 6\omega_g) + k_2} \end{cases} \tag{24}$$

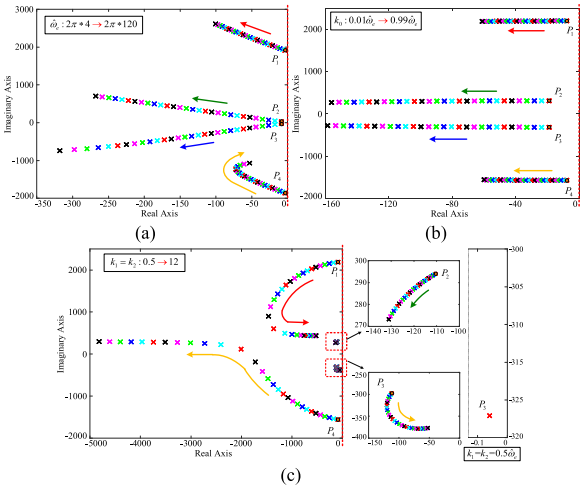

Fig. 8. Pole distribution diagram of the closed-loop transfer function of the proposed M-BESO.

where k_1 and k_2 represent the parameters of the corresponding complex coefficient module, let $k_1 = k_2$; $\hat{x}_{\alpha 2,0}(s)$, $\hat{x}_{\alpha 2,1}(s)$, and $\hat{x}_{\alpha 2,2}(s)$, respectively, represent the fundamental component, harmonic components with angular velocities of $\hat{\omega}_e + 6\omega_g$, and $\hat{\omega}_e - 6\omega_g$ in the estimated BEMF.

Taking the α-axis as an example, the frequency domain expression of the M-BESO can be written as

$$\begin{cases} \varepsilon_{\alpha 1}(s) = \hat{x}_{\alpha 1}(s) - i_{s\alpha}(s) \\ s\hat{x}_{\alpha 1}(s) = \hat{x}_{\alpha 2,0}(s) + \hat{x}_{\alpha 2,1}(s) + \hat{x}_{\alpha 2,2}(s) + b_0 u_{\alpha 0}(s) \\ \qquad + \chi \hat{i}_{s\alpha}(s) - L_1(s) \cdot \varepsilon_{\alpha 1}(s) \\ \hat{x}_{\alpha 2,0}(s) = -L_2(s) \cdot [\varepsilon_{\alpha 1}(s) - \hat{x}_{\alpha 2,1}(s) - \hat{x}_{\alpha 2,2}(s)] \\ \hat{x}_{\alpha 2,1}(s) = G_{+6\omega_g}(s) \cdot [\varepsilon_{\alpha 1}(s) - \hat{x}_{\alpha 2,0}(s) - \hat{x}_{\alpha 2,2}(s)] \\ \hat{x}_{\alpha 2,2}(s) = G_{-6\omega_g}(s) \cdot [\varepsilon_{\alpha 1}(s) - \hat{x}_{\alpha 2,0}(s) - \hat{x}_{\alpha 2,1}(s)]. \end{cases} \tag{25}$$

The $\hat{x}_{\alpha 2,0}(s)$ is the output of the M-BESO. Then, the estimated α-axis BEMF can be expressed as

$$\hat{e}_{s\alpha} = -L_q \hat{x}_{\alpha 2,0}(s). \tag{26}$$

Similarly, the error state equation of the M-BESO is derived based on (25) and (9). According to (25), the following equation can be obtained:

$$\begin{cases} \{s + [L_1(s) - \chi]\} \cdot \varepsilon_{\alpha 1}(s) = \hat{x}_{\alpha 2,0}(s) + \hat{x}_{\alpha 2,1}(s) \\ \qquad + \hat{x}_{\alpha 2,2}(s) - x_{\alpha 2}(s) \\ W(s) = \frac{[s + L_2(s)]}{[L_2(s) - L_2(s) \cdot G_{-6\omega_g}(s)] \cdot [G_{+6\omega_g}(s) - 1]} \\ \varepsilon_{\alpha 1}(s) = \left[1 - G_{+6\omega_g}(s) G_{-6\omega_g}(s)\right] \cdot W(s) \hat{x}_{\alpha 2,0}(s) \\ \qquad + \hat{x}_{\alpha 2,0}(s) \\ \hat{x}_{\alpha 2,1}(s) = \left[G_{+6\omega_g}(s) - G_{+6\omega_g}(s) G_{-6\omega_g}(s)\right] \\ \qquad \cdot W(s) \hat{x}_{\alpha 2,0}(s) \\ \hat{x}_{\alpha 2,2}(s) = \left[G_{-6\omega_g}(s) - G_{+6\omega_g}(s) G_{-6\omega_g}(s)\right] \\ \qquad \cdot W(s) \hat{x}_{\alpha 2,0}(s). \end{cases} \tag{27}$$

According to (27), the transfer function from $\hat{x}_{\alpha 2,0}(s)$ to $x_{\alpha 2}(s)$ can be expressed as (28) shown at the bottom of the next page. By substituting (20) and (24) into (28), the transfer function from the estimated BEMF to the actual BEMF of the M-BESO can be obtained as follows:

$$\begin{aligned} G_M(s) &= \frac{\hat{x}_{\alpha 2,0}(s)}{x_{\alpha 2}(s)} = \frac{\hat{e}_{s\alpha}}{e_{s\alpha}} \\ &= \frac{m_0 s^3 + m_1 s^2 + m_2 s}{n_0 s^4 + n_1 s^3 + n_2 s^2 + n_3 s + n_4} \end{aligned} \tag{29}$$

where

$$\begin{cases} \hat{\omega}_{e1} = \hat{\omega}_e + 6\omega_g, \hat{\omega}_{e2} = \hat{\omega}_e - 6\omega_g, c_1 = k_1 + k_2 \\ \qquad - j(\hat{\omega}_{e1} + \hat{\omega}_{e2}) \\ c_2 = k_1 k_2 - \hat{\omega}_{e1}\hat{\omega}_{e2} - j(k_2\hat{\omega}_{e1} + k_1\hat{\omega}_{e2}) \\ c_3 = 2k_1 k_2 - j(k_2\hat{\omega}_{e1} + k_1\hat{\omega}_{e2}) \\ m_0 = k_0, m_1 = -jk_0(\hat{\omega}_{e1} + \hat{\omega}_{e2}), m_2 = -k_0\hat{\omega}_{e1}\hat{\omega}_{e2} \end{cases} \tag{30}$$

$$\begin{cases} n_0 = 1, n_1 = k_0 k_1 + k_0 k_2 + c_1 + k_0 \\ n_2 = -(2k_0 + 1)(k_1 + k_2 + k_1 k_2) + k_0 c_3 \\ \qquad + c_2 + k_0 c_3 + \hat{\omega}_e^2 \\ n_3 = k_0(k_1 + k_2)\hat{\omega}_e^2 - (2k_0 + 1)c_3 \\ \qquad + k_1 k_2(3k_0 + 2) + k_0 c_2 + c_1\hat{\omega}_e^2 \\ n_4 = [k_0 c_3 - k_1 k_2(2k_0 + 1) + c_2]\,\hat{\omega}_e^2 \end{cases} \tag{31}$$

Fig. 8 is the pole movement trajectory of (29) plotted based on (30) and (31), which can be used to analyze the stability of the M-BESO. Fig. 8(a) shows the pole movement trajectory from $2\pi \times 4$ rad/s to $2\pi \times 120$ rad/s when only the center frequency $\hat{\omega}_e$ increases. According to Fig. 8(a), as $\hat{\omega}_e$ increases, the poles P_1, P_2, and P_3 move toward the left half plane of the real axis. Although the pole P_4 moves to the right, it is still located in the left half plane. Therefore, the proposed M-BESO is stable. Fig. 8(b) depicts the trajectory of pole movement as k_0 increases. The larger k_0, the stronger the stability of M-BESO. Fig. 8(c) shows the pole movement trajectory as the coefficients k_1 and k_2 of the complex coefficient module increase. When k_1 and k_2 increase, the poles P_2 and P_4 shift to the left without affecting the stability of the M-BESO. The poles P_1 and P_3 first move to the left and then to the right, but still remain in the left half plane of the real axis. When $k_1 = k_2$ takes the extreme value $0.5\hat{\omega}_e$, pole P_3 is closest to the right half plane of the real axis and still located on the left half plane of the real axis. Therefore, as k_1 and k_2 increase, the M-BESO remains stable.

C. Analysis of Harmonic Suppression Capability of the M-BESO

The denominator of (28) can be expressed as $H(s)$. The harmonic suppression capability of the M-BESO at specific frequencies is analyzed based on (28) and (29). By defining $s = j(\omega_e + 6\omega_g)$, the frequency response of the harmonic with angular velocity $\omega_e + 6\omega_g$ can be obtained, as shown in (32) shown at the bottom of the next page. It is obvious that $H(s)$ is not zero. Therefore, the M-BESO can eliminate the harmonic of angular velocity $\omega_e + 6\omega_g$ in the BEMF. Similarly, analyzing the frequency response of harmonics with angular velocity $\hat{\omega}_e - 6\omega_g$, the M-BESO can suppress harmonics with angular velocity $\hat{\omega}_e - 6\omega_g$.

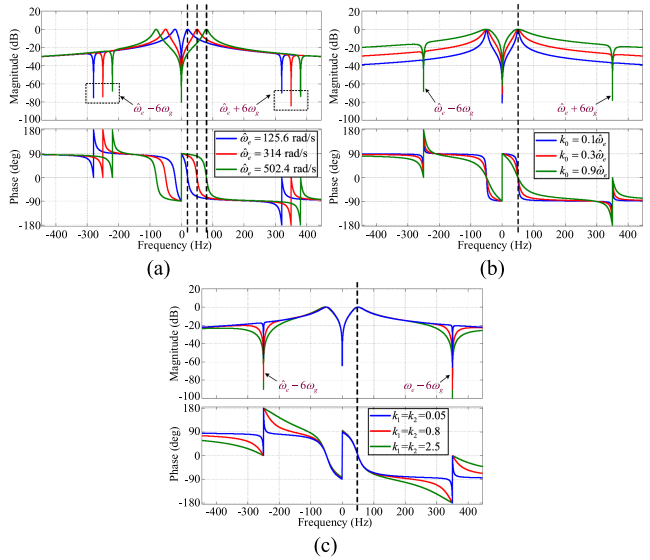

Fig. 9. Bode diagram of the closed-loop transfer function of the proposed M-BESO. (a) When $\hat{\omega}_e$ change. (b) When k_0 change. (c) When k_1, k_2 change.

D. Parameter Design Principles of the M-BESO

The bode diagram of the M-BESO based on (29)–(31) is shown in Fig. 9. When only the center frequency changes, the proposed M-BESO can accurately estimate the BEMF and accurately suppress the harmonics generated by the dc-link voltage harmonic in the BEMF. According to Figs. 8(b) and 9(b), increasing k_0 can enhance stability and improve dynamic performance. However, the overall harmonic suppression capability will weaken, and the estimated noise in BEMF will increase. Therefore, the selection of k_0 should be a compromise between stability and harmonic suppression. According to Fig. 9(c), increasing k_1 and k_2 will enhance the suppression ability of harmonics with angular velocity $\hat{\omega}_e \pm 6\omega_g$ in the BEMF and increase the range of harmonic suppression. But as k_1 and k_2 increase, the stability of M-BESO will deteriorate.

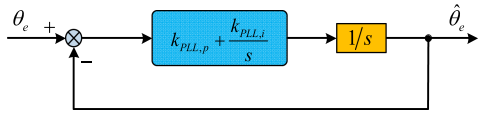

Fig. 10. Equivalent control structure diagram of the TPLL.

E. Design of the IPLL

According to the structure diagram of TPLL in Fig. 2, it can be transformed into the equivalent closed-loop structure diagram in Fig. 10.

From Fig. 10, the transfer function from $\hat{\theta}_e$ to θ_e in TPLL is

$$G_{\mathrm{TPLL}}(s) = \frac{\hat{\theta}_e}{\theta_e} = \frac{k_{\mathrm{PLL},p}s + k_{\mathrm{PLL},i}}{s^2 + k_{\mathrm{PLL},p}s + k_{\mathrm{PLL},i}}. \tag{33}$$

Further, the error transfer function of TPLL is

$$E_{\mathrm{TPLL}}(s) = \frac{\theta_e - \hat{\theta}_e}{\theta_e} = \frac{s^2}{s^2 + k_{\mathrm{PLL},p}s + k_{\mathrm{PLL},i}}. \tag{34}$$

In [28], it is pointed out that when the input is a ramp frequency signal, TPLL will generate estimation errors. According to the terminal value theorem, it can be derived that

$$\begin{aligned}\lim_{t\to\infty} e_{TPLL}(t) &= \lim_{s\to 0} sE_{\mathrm{TPLL}}(s)\frac{B}{s^3} \\ &= \lim_{s\to 0} s\frac{s^2}{s^2 + k_{\mathrm{PLL},p}s + k_{\mathrm{PLL},i}}\frac{B}{s^3} = \frac{B}{k_{\mathrm{PLL},i}}\end{aligned} \tag{35}$$

where B represents the amplitude of the ramp frequency signal. In this article, the structure of IPLL is designed based on third-order ESO to eliminate the aforementioned positional errors. Consider the following second-order system:

$$\begin{cases}\dot{\theta}_e = \omega_e \\ \dot{\omega}_e = a_e\end{cases} \tag{36}$$

where a_e represents angular acceleration. There is a derivative relationship between the angular acceleration, angular speed, and electrical angle of the motor. Therefore, taking a_e as an

$$\begin{aligned}&\frac{\hat{x}_{\alpha 2,0}(s)}{x_{\alpha 2}(s)} \\ &= \frac{L_2(s)\cdot\left[1 - G_{+6\omega_g}(s)\right]\left[1 - G_{-6\omega_g}(s)\right]}{\{s + [L_1(s) - \chi]\}\left\{[s + L_2(s)]\cdot\left[1 - G_{+6\omega_g}(s)G_{-6\omega_g}(s)\right] + L_2(s)\cdot\left[1 - G_{+6\omega_g}(s)\right]\left[G_{-6\omega_g}(s) - 1\right]\right\} + L_2(s)} \\ &\quad \cdot\left[1 - G_{+6\omega_g}(s)\right]\left[G_{-6\omega_g}(s) - 1\right] + [s + L_2(s)]\left[2G_{+6\omega_g}(s)G_{-6\omega_g}(s) - G_{+6\omega_g}(s) - G_{-6\omega_g}(s)\right]\end{aligned} \tag{28}$$

$$\begin{aligned}G_M\left[j(\omega_e + 6\omega_g)\right] &= \lim_{\hat{\omega}_e\to\omega_e} \frac{L_2(s)\cdot\left[1 - G_{+6\omega_g}(s)\right]\left[1 - G_{-6\omega_g}(s)\right]}{H(s)} \\ &= \lim_{\hat{\omega}_e\to\omega_e} \frac{L_2\left[j(\omega_e + 6\omega_g)\right]\cdot\{1 - k_1/[j(\omega_e + 6\omega_g) - j(\hat{\omega}_e + 6\omega_g) + k_1]\}\{1 - k_2/[j(\omega_e + 6\omega_g) - j(\hat{\omega}_e - 6\omega_g) + k_2]\}}{H\left[j(\omega_e + 6\omega_g)\right]} \\ &= 0.\end{aligned} \tag{32}$$

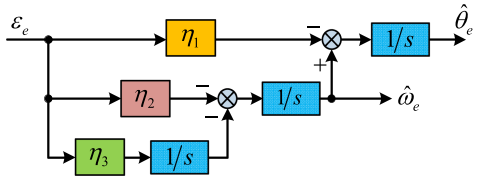

Fig. 11. Control structure diagram of the IPLL based on the third-order ESO.

extended perturbation variable, the following third-order ESO is obtained:

$$\begin{cases} \varepsilon_e = \hat{y}_1 - \theta_e \\ p\hat{y}_1 = \hat{y}_2 - \eta_1\varepsilon_e \\ p\hat{y}_2 = \hat{y}_3 - \eta_2\varepsilon_e \\ p\hat{y}_3 = -\eta_3\varepsilon_e \end{cases} \tag{37}$$

where $\hat{y}_1$, $\hat{y}_2$, and $\hat{y}_3$ represent the estimated variables of θ_e, ω_e, and a_e, respectively; η_1, η_2, and η_3 are the gain coefficients of third-order ESO.

The control structure diagram of the IPLL based on the third-order ESO is presented in Fig. 11. According to (37), the frequency domain expression can be obtained. Derive the frequency domain expression to obtain the transfer function of IPLL as follows:

$$G_{\text{TPLL}}(s) = \frac{\hat{\theta}_e}{\theta_e} = \frac{\eta_1 s^2 + \eta_2 s + \eta_3}{s^3 + \eta_1 s^2 + \eta_2 s + \eta_3}. \tag{38}$$

Furthermore, the error transfer function of IPLL is

$$E_{\text{IPLL}}(s) = \frac{\theta_e - \hat{\theta}_e}{\theta_e} = \frac{s^3}{s^3 + \eta_1 s^2 + \eta_2 s + \eta_3}. \tag{39}$$

When the input is the ramp frequency signal, according to the terminal value theorem, the estimation error of IPLL is

$$\begin{aligned} \lim_{t\to\infty} e_{\text{IPLL}}(t) &= \lim_{s\to 0} sE_{\text{IPLL}}(s)\frac{B}{s^3} \\ &= \lim_{s\to 0} s\frac{s^3}{s^3 + \eta_1 s^2 + \eta_2 s + \eta_3}\frac{B}{s^3} = 0. \end{aligned} \tag{40}$$

Therefore, when the motor speed changes rapidly, the proposed IPLL has higher rotor position estimation accuracy compared to TPLL. According to (38), the characteristic equation of IPLL can be obtained. To simplify the principle of parameter tuning, the three poles of the characteristic equation can be assigned to the same point, as follows:

$$s^3 + \eta_1 s^2 + \eta_2 s + \eta_3 = (s + r)^3 \tag{41}$$

where r is the bandwidth of the third-order ESO. Then

$$\begin{cases} \eta_1 = 3r \\ \eta_2 = 3r^2 \\ \eta_3 = r^3. \end{cases} \tag{42}$$

IV. Experimental Verification

On the experimental platform of 2 kW PMSM electrolytic capacitorless driver in Fig. 12, the proposed method is transformed into software code for verification. All software algorithms are implemented in the TMS320F28335 chip developed by Texas Instruments. The sensorless control algo-rithm is executed in pulsewidth modulation (PWM) interrupts in the PMSM electrolytic capacitorless drives. The switching frequency of power devices and the frequency of PWM interruption are both 4 kHz. Table I shows the parameters of the test motor in the experimental platform, which is IPMSM. The loading PMSM is controlled by the servo driver to provide load torque. The control structure block diagram of the sensorless control method proposed in this article is depicted as Fig. 13. In the experimental verification part, the comparative experiments of the TESO, BESO, and M-BESO are carried out to show the advantages of the proposed M-BESO. In the speed and position estimation, the performance of TPLL and IPLL is compared during the rapid change of motor speed. The bandwidth of the TESO is set to: $\omega_0 = 2000$ rad/s. The parameter of the BESO is: $k_0 = 0.6\,\hat{\omega}_e$. The parameters of the M-BESO are: $k_0 = 0.6\,\hat{\omega}_e$ and $k_1 = k_2 = 1.5$.

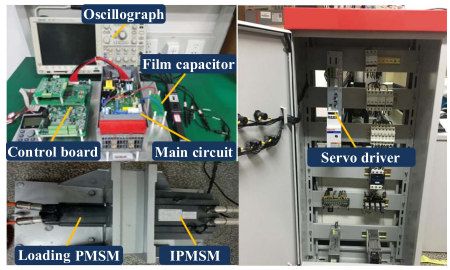

Fig. 12. Schematic diagram of the experimental platform for the PMSM electrolytic capacitorless drives.

TABLE I
PMSM Parameters

Parameter	value	Parameter	value
Rated voltage	380 V	Rated current	5.8 A
Rated power	2 kW	Rated torque	19 N·m
Rated speed	1000 rpm	Rated frequency	66.67 Hz

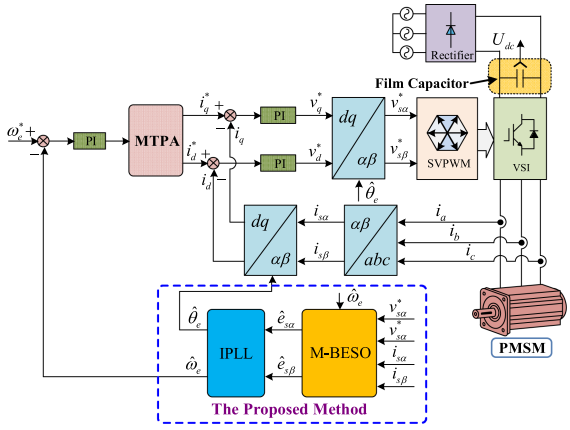

Fig. 13. Overall control diagram of the proposed sensorless control method in this article.

A. Performance Comparison of Different PLLs and ESOs

Fig. 14 captures the experimental data when the motor speed rapidly changes at 250-400-550-700-850-1000-250 r/min. For electrolytic capacitorless drives, rapid deceleration can easily

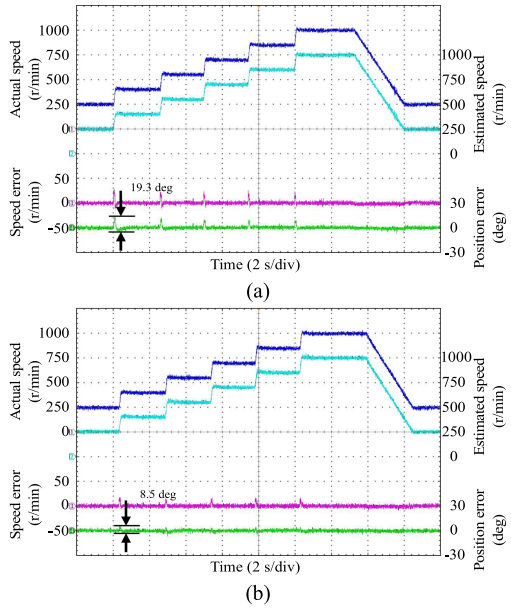

Fig. 14. Experimental waveforms of using different PLLs based on M-BESO sensorless method during rapid motor acceleration. (a) M-BESO+TPLL. (b) M-BESO+IPLL.

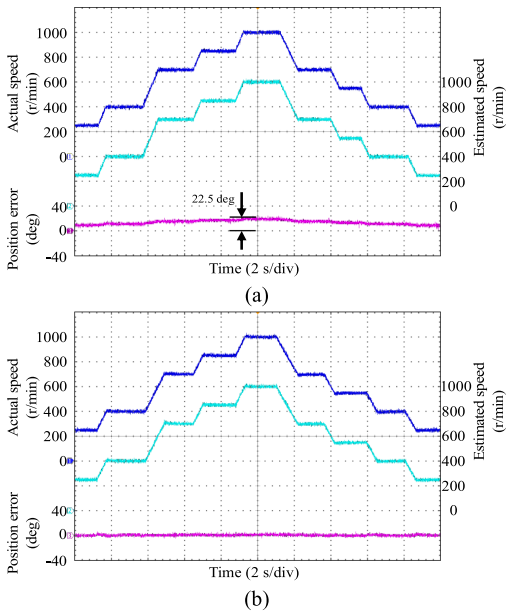

Fig. 15. Experimental results using different ESOs based on IPLL during acceleration and deceleration. (a) TESO+IPLL. (b) M-BESO+IPLL.

trigger dc-link overvoltage. Therefore, only the position estimation performance of different PLLs during rapid acceleration is validated in this article. Both TPLL and IPLL rely on M-BESO to estimate motor BEMF. According to Fig. 14(a), when using TPLL, the maximum position error during rapid acceleration is 19.3°. As shown in Fig. 14(b), when using the designed IPLL, the speed error and position error are significantly reduced. The maximum positional difference is only 8.5°.

Fig. 15 shows the experimental results of using different ESOs based on IPLL during motor acceleration and deceleration. The TESO exhibits low-pass filtering characteristics, and the estimated BEMF phase lag increases with the increase of motor speed. According to Fig. 15(a), the position error increases with the increase of motor speed, and the maximum position error is 22.5°. And M-BESO has no phase lag at the center frequency. According to the experimental waveform in Fig. 15(b), the position estimation error using M-BESO during motor acceleration and deceleration is relatively small and the variation is small.

B. Performance Verification of Harmonic Suppression

Fig. 16 shows experimental waveforms using different sensorless control methods when the motor operates at 1000 r/min and applies rated load. For electrolytic capacitorless drives, only when the motor is operating with the load, the dc-link voltage will show significant fluctuations. To compare the performance of different ESO, all three sensorless control methods use IPLL to obtain rotor position information. According to Fig. 16(a), there is significant distortion in the BEMF estimated by TESO. According to the fast Fourier transform (FFT) results, the TESO is unable to effectively suppress BEMF harmonics. Due to the phase lag of the BEMF estimated by TESO, the maximum position error is 18.2°. And the fluctuation range of position error caused by BEMF harmonics is 9.5°. From Fig. 16(b), it can be seen that the BESO can effectively reduce the phase lag of estimated BEMF. However, the BESO needs to compromise between dynamic performance and harmonic suppression. According to the FFT results, the BESO is unable to completely suppress the BEMF harmonics. The maximum position error is 7.8°, and the fluctuation range of position error is 5.6°. From the experimental waveform in Fig. 16(c), it can be seen that there is almost no distortion in the BEMF, and harmonics are effectively suppressed. The rotor position estimation error is further reduced, with the maximum position error of only 5.1° and position error fluctuation range of 2.3°. Therefore, the proposed M-BESO can accurately estimate the BEMF while effectively suppressing the BEMF harmonics caused by the ac component of the dc-link voltage, reducing the position estimation error.

Fig. 17 shows the experimental results of the motor running at 600 r/min and applies rated load. According to Fig. 17(a), there is distortion in the BEMF estimated by TESO. During the operation of the motor with load, the maximum position error is 10.2°. The BEMF harmonics cause rotor position estimation errors, with the position error fluctuation range of 8.4°. Fig. 17(b) shows that the BESO has limited ability to suppress BEMF harmonics. The harmonics in the BEMF still cause position estimation errors, with the maximum position error of 6.1° and position error fluctuation range of 4.2°. According to Fig. 17(c), the proposed M-BESO can effectively suppress BEMF harmonics and reduce position estimation errors. The maximum position error is 5.2°, and the fluctuation range of position error is only 2.2°.

Experimental waveforms using different sensorless control methods when the motor operates at 150 r/min and applies rated load are Fig. 18. When the motor speed is 150 r/min, the motor frequency is 10 Hz. For the TESO, the lower the motor operating frequency, the smaller the estimated BEMF phase lag. According to Fig. 18(a), the maximum position error is 8.3°. And the rotor position error contains fluctuation components.

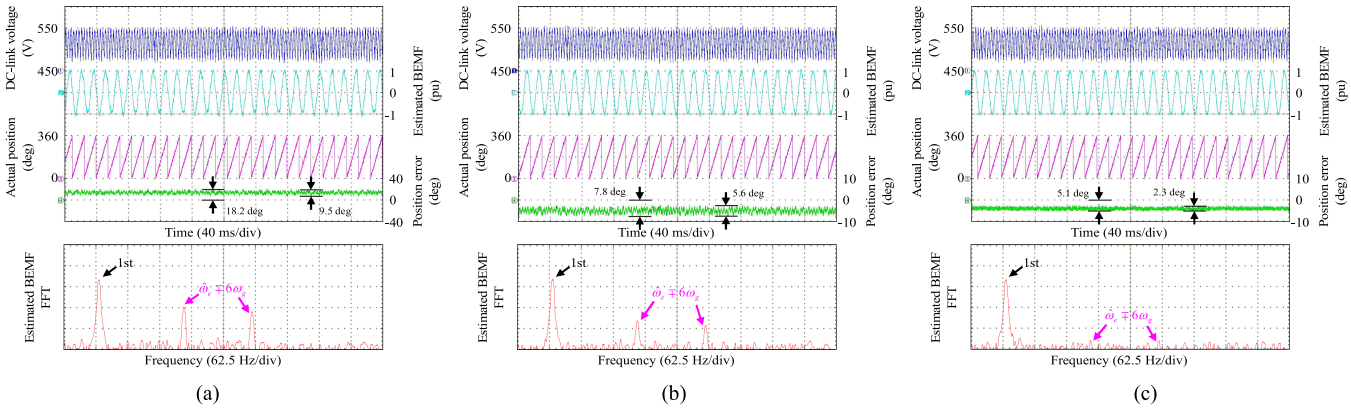

Fig. 16. Experimental waveforms using different sensorless control methods when the motor operates at 1000 r/min and applies rated load. (a) TESO+IPLL. (b) BESO+IPLL. (c) M-BESO+IPLL.

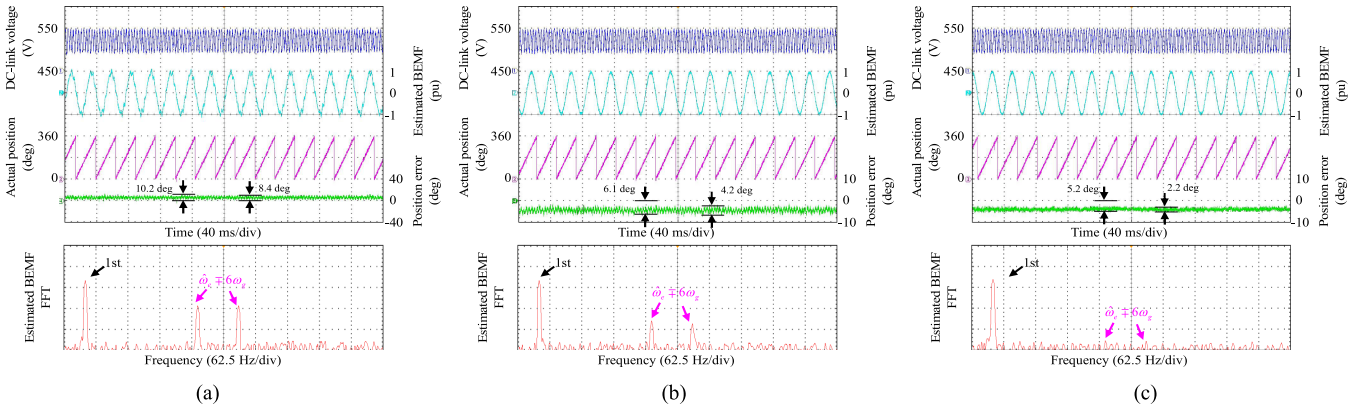

Fig. 17. Experimental waveforms using different sensorless control methods when the motor operates at 600 r/min and applies rated load. (a) TESO+IPLL. (b) BESO+IPLL. (c) M-BESO+IPLL.

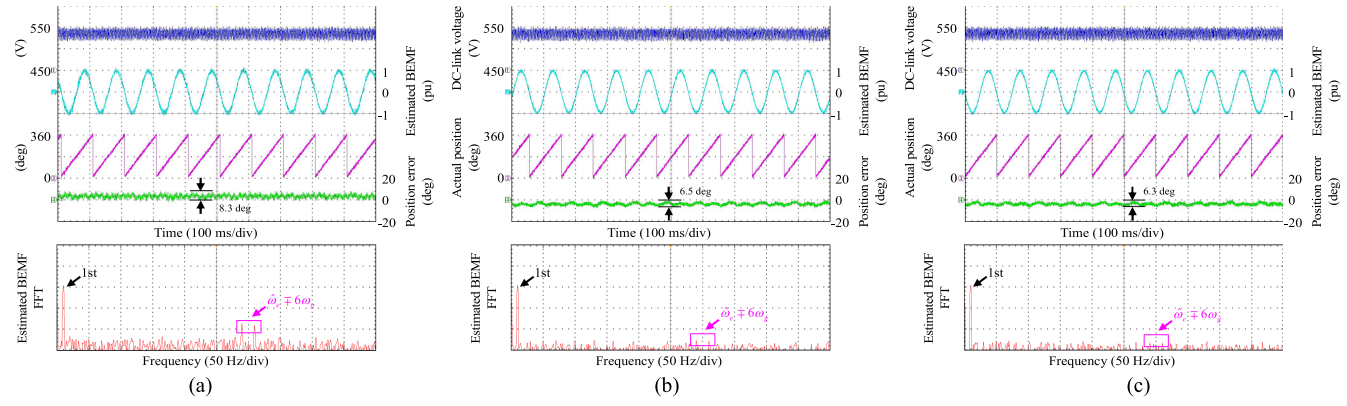

Fig. 18. Experimental waveforms using different sensorless control methods when the motor operates at 150 r/min and applies rated load. (a) TESO+IPLL. (b) BESO+IPLL. (c) M-BESO+IPLL.

From the FFT results, the TESO is unable to effectively suppress BEMF harmonics. For electrolytic capacitorless drives, the harmonic frequencies generated by the dc-link voltage ac component in BEMF are −290 and 310 Hz, respectively. The harmonic frequency is far away from the motor frequency of the, so both sensorless control methods based on the BESO and M-BESO can effectively suppress BEMF harmonics. According to Fig. 18(b) and (c), the maximum position estimation errors when using two sensorless control methods are 6.5° and 6.3°, respectively.

From the above experimental data, it can be seen that the proposed M-BESO has higher position estimation accuracy and better harmonic suppression ability compared to the BESO and TESO.

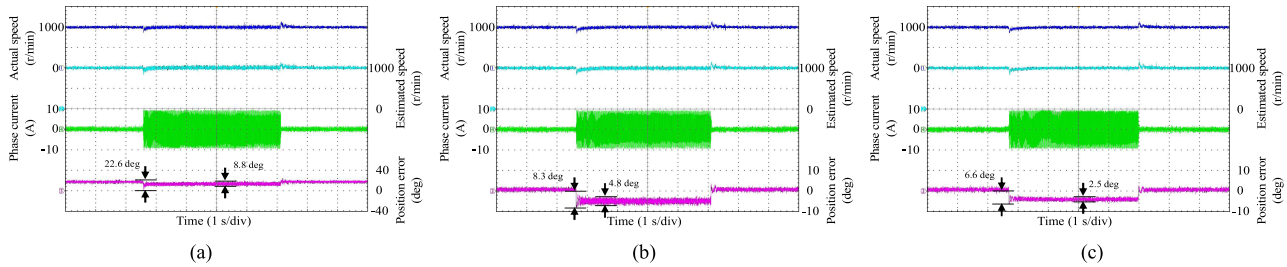

Fig. 19. Experimental waveforms using different sensorless control methods when the motor is running at 1000 r/min and suddenly changes the rated load. (a) TESO+IPLL. (b) BESO+IPLL. (c) M-BESO+IPLL.

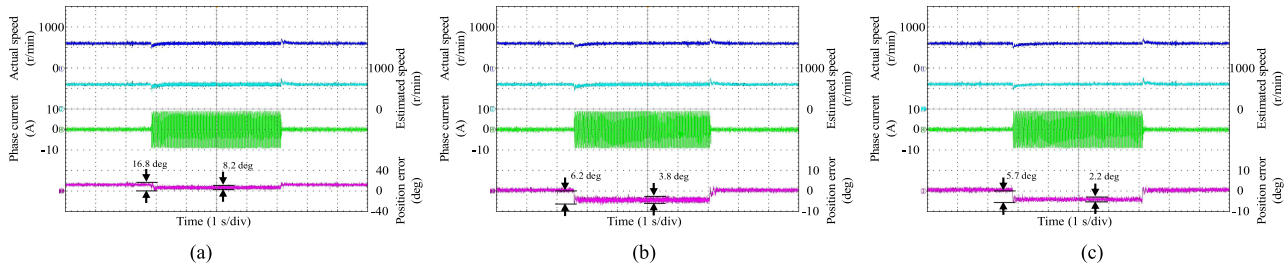

Fig. 20. Experimental waveforms using different sensorless control methods when the motor is running at 600 r/min and suddenly changes the rated load. (a) TESO+IPLL. (b) BESO+IPLL. (c) M-BESO+IPLL.

C. Performance Comparison During Sudden Load Changes

Fig. 19 collects the experimental results using TESO, BESO, and M-BESO when the motor is running at 1000 r/min and suddenly subjected to rated load disturbance. According to Fig. 19(a), during the load change process, the maximum position error using TESO is 22.6° and the fluctuation range of position error during the application of load is 8.8°. From Fig. 19(b), the BESO can effectively reduce the lag in estimating BEMF, with the maximum position error of 8.3° when using BESO. However, the BESO is unable to completely suppress the BEMF harmonics, and the fluctuation range of position error during load application is 4.8°. According to Fig. 19(c), the maximum position error when using M-BESO is 6.6° and during the application of load, the fluctuation range of position error is reduced to 2.5°. Therefore, according to the experimental results, the proposed M-BESO can effectively reduce the phase lag of estimated BEMF compared to the TESO. Meanwhile, compared to the TESO and BESO, the M-BESO can effectively suppress harmonics in the estimated BEMF, thereby reducing position estimation errors.

Fig. 20 shows experimental waveforms using different sensorless control methods when the motor is running at 600 r/min and suddenly subjected to rated load disturbances. During the process of load change, the estimated BEMF by TESO exhibits phase lag and is difficult to suppress BEMF harmonics. The maximum position error is 16.8°, and the fluctuation range of position error during the application of load is 8.2°. According to Fig. 20(b), the maximum position error when using BESO is 6.2°. During the application of load, the fluctuation range of position error is 3.8°. The harmonics still exist in the BEMF estimated by BESO, causing fluctuations in position estimation errors. According to Fig. 20(c), when using the proposed M-BESO, the maximum position error and position error fluctuation range are reduced to 5.7° and 2.2°, respectively. Therefore, the proposed M-BESO outperforms BESO in BEMF harmonic suppression.

Fig. 21 depicts the experimental results using TESO, BESO, and M-BESO when the motor is working at 150 r/min and suddenly subjected to rated load disturbance. As the motor speed decreases, the signal-to-noise ratio of the BEMF signal decreases and the noise increases accordingly. However, the bandwidth of TESO is fixed, making it difficult to suppress the impact of noise. According to Fig. 21(a), when TESO is used, the fluctuation range of position error during the loading process is 7.1°. From Fig. 21(b) and (c), when using BESO and M-BESO, position error fluctuation range is reduced to 4.5° and 4.3°, respectively. For the BESO and the M-BESO, the bandwidth coefficient of the BEMF fundamental component estimation module varies with the motor operating frequency, which can effectively eliminate the influence of noise. In addition, the proposed BESO and M-BESO exhibit no phase shift or amplitude attenuation at the center frequency, and can effectively alleviate BEMF harmonics.

D. Performance Verification of DC Component Suppression

Fig. 22 shows the experimental waveforms when TESO and M-BESO are used to superimpose dc components on the α-axis voltage. When Flag $=1$, add a 4 V dc component. The transfer function of the TESO exhibits low-pass filtering characteristics. Therefore, it is difficult to effectively solve the influence of dc components. According to Fig. 22(a), when Flag $=1$, the α-axis BEMF generates a dc bias, and the position estimation error of TESO increases, with a maximum position error of 16.3°.

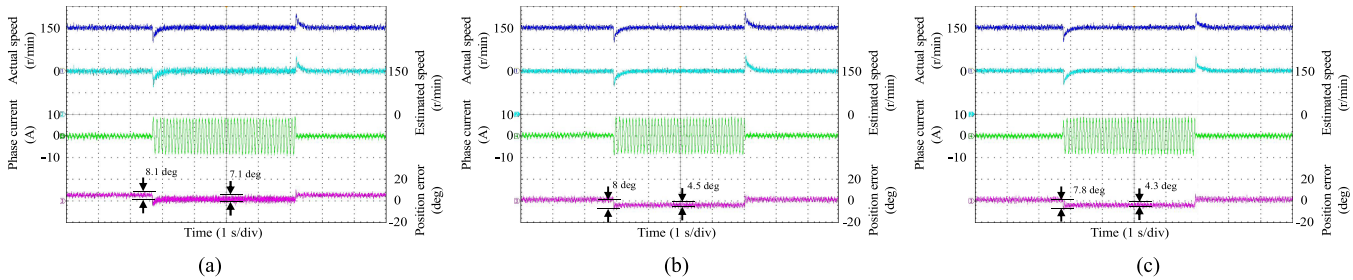

Fig. 21. Experimental waveforms using different sensorless control methods when the motor is running at 150 r/min and suddenly changes the rated load. (a) TESO+IPLL. (b) BESO+IPLL. (c) M-BESO+IPLL.

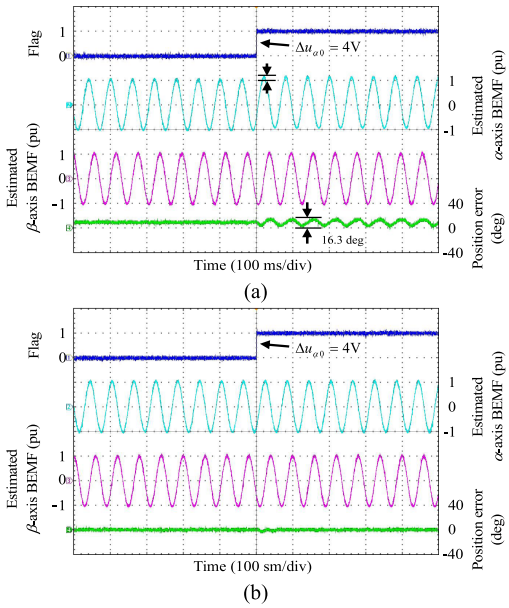

Fig. 22. Experimental waveforms using different sensorless control methods when the motor operates at 250 r/min and a dc component of 4 V is applied to the α-axis voltage. (a) TESO+IPLL. (b) M-BESO+IPLL.

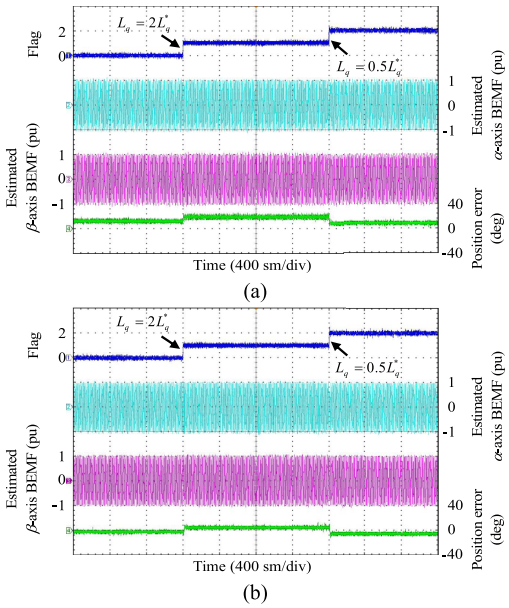

Fig. 23. Experimental results of inductance mismatch when the motor operates at 1000 r/min. (a) TESO+IPLL. (b) M-BESO+IPLL.

From Fig. 22(b), the proposed M-BESO can effectively suppress the influence of the dc component. The α-axis BEMF hardly generates dc bias and the position error is not affected.

E. Performance Verification of Motor Parameter Mismatch

Fig. 23 shows the experimental results of q-axis inductance parameter mismatch when the motor operates at 1000 r/min. When Flag $= 1$, the q-axis inductance becomes twice the nominal value; When Flag $= 2$, the q-axis inductance becomes half of the nominal value. According to Fig. 23, it can be seen that q-axis inductance mismatch will result in significant positional errors. Fig. 24 shows the experimental waveform of resistance parameter mismatch when the motor operates at 150 r/min. The stator resistance is changed to twice and half of the nominal value, respectively. According to the experimental waveform, stator resistance mismatch will change the amplitude of estimated BEMF, but has little effect on the estimated position. During the process of stator resistance variation, there is no significant change in position error.

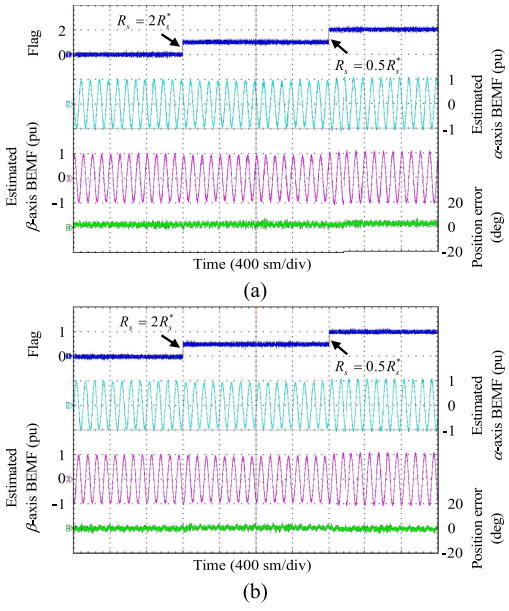

Fig. 24. Experimental results of resistance mismatch when the motor operates at 150 r/min. (a) TESO+IPLL. (b) M-BESO+IPLL.

V. Conclusion

The TESO is difficult to accurately estimate the BEMF of sinusoidal variations and effectively suppress the BEMF harmonics caused by fluctuating dc-link voltages. Therefore, the sensorless control strategy for PMSM electrolytic capaci-torless driver based on the M-BESO is proposed in this article. The M-BESO is used to accurately estimate the BEMF of the motor. In addition, to reduce the position estimation error when the motor speed changes rapidly, an IPLL based on third-order ESO is designed. Compared to the TESO, the M-BESO has no phase shift or amplitude attenuation at the center frequency, allowing for accurate estimation of motor BEMF and the M-BESO can effectively suppress BEMF harmonics generated by dc-link voltage, as well as suppress dc bias. Finally, the effectiveness of IPLL and M-BESO is validated on the 2 kW PMSM electrolytic capacitorless driver experimental platform.

References

[1] S. Bhattacharjee, S. Halder, Y. Yan, A. Balamurali, L. V. Iyer, and N. C. Kar, "Real-time SIL validation of a novel PMSM control based on deep deterministic policy gradient scheme for electrified vehicles," *IEEE Trans. Power Electron.*, vol. 37, no. 8, pp. 9000–9011, Aug. 2022.

[2] H. Gao, Z. Zhang, Y. Liu, W. Huang, and H. Xue, "Development and analysis of dual three-phase PMSM with phase-shifted hybrid winding for aircraft electric propulsion application," *IEEE Trans. Transp. Electrific.*, vol. 10, no. 3, pp. 6497–6508, Sep. 2024.

[3] C. Li, Z. Wang, and Y. Xu, "A wireless-power-transfer-based three-phase PMSM drive system with matrix converter," *IEEE Trans. Ind. Electron.*, vol. 70, no. 3, pp. 2307–2317, Mar. 2023.

[4] A. V. Deshmukh, M. Afshar, S. Jena, A. M. Hava, Z. Yu, and B. Akin, "A practical control method for single-phase input PMSM drives with small DC-link capacitor," *IEEE Trans. Power Electron.*, vol. 40, no. 3, pp. 4358–4373, Mar. 2025, doi: 10.1109/TPEL.2024.3503475.

[5] Z. Ren et al., "Adaptive virtual admittance reshaping-based resonance suppression strategy for PMSM drives with small DC-link capacitor," *IEEE Trans. Power Electron.*, vol. 39, no. 3, pp. 3109–3121, Mar. 2024.

[6] R. Gao, Z. Fu, D. Ding, G. Wang, G. Zhang, and D. Xu, "Beat phenomenon feature extraction based harmonic decoupling for electrolytic capacitorless motor drives," *IEEE Trans. Ind. Electron.*, vol. 72, no. 2, pp. 1193–1204, Feb. 2025, doi: 10.1109/TIE.2024.3404145.

[7] Y. Lu, B. Zhou, Y. Zhang, and Q. Chang, "Doubly salient electromagnetic motor-drive system with small DC-link capacitance," *IEEE Trans. Ind. Electron.*, vol. 71, no. 8, pp. 9373–9382, Aug. 2024.

[8] G. Wang, M. Valla, and J. Solsona, "Position sensorless permanent magnet synchronous machine drives—A review," *IEEE Trans. Ind. Electron.*, vol. 67, no. 7, pp. 5830–5842, Jul. 2020.

[9] X. Li et al., "Low-speed rotating restart and speed recording for free-running sensorless IPMSM based on ultrahigh frequency sinusoidal wave injection," *IEEE Trans. Power Electron.*, vol. 37, no. 12, pp. 15245–15259, Dec. 2022.

[10] Z. Wang, C. Gao, M. Gu, and M. Cheng, "A novel vector magnetic circuit based position observer for IPMSM drives using high-frequency signal injection," *IEEE Trans. Power Electron.*, vol. 39, no. 1, pp. 1333–1342, Jan. 2024.

[11] X. Sun, Y. Zhang, X. Tian, J. Cao, and J. Zhu, "Speed sensorless control for IPMSMs using a modified MRAS with gray wolf optimization algorithm," *IEEE Trans. Transp. Electrific.*, vol. 8, no. 1, pp. 1326–1337, Mar. 2022.

[12] F. Gao, Z. Yin, P. Zhang, Y. Zhang, and Y. Zhang, "A position sensorless control method robust to inductance mismatch for SynRM based on generalized multiple model resonant kalman filter," *IEEE Trans. Power Electron.*, vol. 39, no. 5, pp. 5510–5521, May 2024.

[13] T. Wang, B. Wang, Y. Yu, and D. Xu, "High-order sliding-mode observer with adaptive gain for sensorless induction motor drives in the wide-speed range," *IEEE Trans. Ind. Electron.*, vol. 70, no. 11, pp. 11055–11066, Nov. 2023.

[14] J. Zhu, Q. Ge, and P. Sun, "Extended State observer-based sensorless control for high-speed maglev application in single-feeding mode and double-feeding mode," *IEEE Trans. Transp. Electrific.*, vol. 8, no. 1, pp. 1350–1361, Mar. 2022.

[15] Z. Xu, T. Zhang, Y. Bao, H. Zhang, and C. Gerada, "A nonlinear extended State observer for rotor position and speed estimation for sensorless IPMSM drives," *IEEE Trans. Power Electron.*, vol. 35, no. 1, pp. 733–743, Jan. 2020.

[16] F. Jiang et al., "Robustness improvement of model-based sensorless SPMSM drivers based on an adaptive extended state observer and an enhanced quadrature PLL," *IEEE Trans. Power Electron.*, vol. 36, no. 4, pp. 4802–4814, Apr. 2021.

[17] Y. Zhang, Z. Yin, C. Bai, G. Wang, and J. Liu, "A rotor position and speed estimation method using an improved linear extended State observer for IPMSM sensorless drives," *IEEE Trans. Power Electron.*, vol. 36, no. 12, pp. 14062–14073, Dec. 2021.

[18] Z. Xia, X. Yu, X. Wu, and Y. Dou, "An enhanced linear extended State observer-based sensorless IPMSM drives with robustness against current measurement offset error," *IEEE Trans. Transp. Electrific.*, vol. 11, no. 1, pp. 3558–3567, Feb. 2025, doi: 10.1109/TTE.2024.3443809.

[19] P. Du, B. Wang, and D. Xu, "A minimum-order BEMF observer for DC-bias elimination of position-sensorless PMSM drives using backstepping design," *IEEE Trans. Ind. Electron.*, vol. 71, no. 11, pp. 13635–13649, Nov. 2024.

[20] G. Wang, X. Yi, and H. Lin, "Adaptive generalized complex vector observer for sensorless control of PMSM with robustness to current measurement errors," *IEEE Trans. Ind. Electron.*, vol. 71, no. 12, pp. 15313–15324, Dec. 2024.

[21] Y. Li, Z. Yin, Y. Zhang, Y. Gao, J. Liu, and P. Zhang, "A harmonic suppression strategy based on adaptive synchronous rotating frame transformation for improving the estimation accuracy of sensorless drivers with small capacitors," *IEEE Trans. Power Electron.*, vol. 39, no. 3, pp. 3521–3532, Mar. 2024.

[22] X. Wu et al., "Improved position observer using adaptive training control-based filter for interior permanent magnet synchronous motor drives," *IEEE Trans. Power Electron.*, vol. 38, no. 8, pp. 10128–10137, Aug. 2023.

[23] G. Wang, H. Zhan, G. Zhang, X. Gui, and D. Xu, "Adaptive compensation method of position estimation harmonic error for EMF-based observer in sensorless IPMSM drives," *IEEE Trans. Power Electron.*, vol. 29, no. 6, pp. 3055–3064, Jun. 2014.

[24] J. Huo, N. Zhao, R. Gao, G. Zhang, G. Wang, and D. Xu, "Analysis and compensation of position estimation error for sensorless reduced DC-link capacitance IPMSM drives," *IEEE Trans. Ind. Electron.*, vol. 70, no. 3, pp. 3213–3221, Mar. 2023.

[25] H. Cheng, S. Sun, X. Zhou, D. Shao, S. Mi, and Y. Hu, "Sensorless DPCC of PMLSM using SOGI-PLL-based high-order SMO with cogging force feedforward compensation," *IEEE Trans. Transp. Electrific.*, vol. 8, no. 1, pp. 1094–1104, Mar. 2022.

[26] B. Wang, P. Du, M. Tian, and D. Xu, "A master-slave-structure position observer for multiharmonics suppression in sensorless PMSM drives," *IEEE Trans. Ind. Electron.*, vol. 71, no. 5, pp. 4528–4540, May 2024.

[27] P. Du, B. Wang, and D. Xu, "A BEMF harmonic-extended State $\gamma\delta$-axes observer for PMSM sensorless control reducing structural redundancy," *IEEE Trans. Ind. Electron.*, vol. 72, no. 5, pp. 4623–4638, May 2025.

[28] H. Wang, Y. Yang, X. Ge, Y. Zuo, Y. Yue, and S. Li, "PLL- and FLL-based speed estimation schemes for speed-sensorless control of induction motor drives: Review and new attempts," *IEEE Trans. Power Electron.*, vol. 37, no. 3, pp. 3334–3356, Mar. 2022.

Yuehan Li was born in Shaanxi, China, in 1998. He received the B.S. degree in electrical engineering in 2020 from the Xi'an University of Technology, Xi'an, China, where he is currently working toward the Ph.D. degree in electrical engineering.

His current research focuses on high performance control of permanent magnet synchronous motor.

Zhonggang Yin (Member, IEEE) was born in Shandong, China, in 1982. He received the B.S., M.S., and Ph.D. degrees in electrical engineering from the Xi'an University of Technology, Xi'an, China, in 2003, 2006, and 2009, respectively.

In 2009, he joined the Electrical Engineering Department, Xi'an University of Technology, where he is currently a Professor. His research interests include high-performance control of ac motor and digital control of power converters.

Dongsheng Yuan received the B.S. and M.S. degrees in electrical engineering from Lanzhou Jiaotong University, Lanzhou, China, in 2010 and 2014, and the Ph.D. degree in electrical engineering from Xi'an Jiaotong University, Xi'an, China, in 2020.

From 2017 to 2019, he was a visiting student with the Department of Electrical Engineering and Computer Science, University of Tennessee, Knoxville, TN, USA. In 2020, he joined the Electrical Engineering Department, Xi'an University of Technology. His research interests include electromagnetic devices and fast functional modeling of power converter systems.

Yanqing Zhang (Member, IEEE) received the B.S., M.S., and Ph.D. degrees in electrical engineering from the Xi'an University of Technology, Xi'an, China, in 2012, 2015, and 2019, respectively.

In 2019, he joined the School of Electrical Engineering, Xi'an University of Technology, where he is currently an Associate Professor. His research focuses on high performance control of ac motor.

Yixuan Gao was born in Shaanxi, China, in 1998. He received the B.S. degree in electrical engineering in 2020 from the Xi'an University of Technology, Xi'an, China, where he is currently working toward the Ph.D. degree in electrical engineering.

His research focuses on high performance control of servo motor.

Hui Yang received the B.S., M.S., and Ph.D. degrees in electrical engineering from the Xi'an University of Technology, Xi'an, China, in 2001, 2007, and 2018, respectively.

Since 2004, she has been with the Xi'an University of Technology, where she is currently an Assistant Professor with the School of Electrical Engineering. From 2019 to 2020, she was a Visiting Scholar with FEEC of Virginia Tech University, Blacksburg, VA, USA. Her research interests include distributed power systems, digital control of power converters, and energy storage systems.